

Study of magnetic anisotropy and magnetization reversal using the quadratic magneto-optical effect in epitaxial $\text{Co}_x\text{Mn}_y\text{Ge}_z$ (111) films

P K Muduli^{1,3}, W C Rice¹, L He¹, B A Collins¹, Y S Chu^{2,4}
and F Tsui¹

¹ Department of Physics and Astronomy, University of North Carolina, Chapel Hill, NC 27599, USA

² Advanced Photon Source, Argonne National Laboratory, Argonne, IL 60439, USA

E-mail: ftsui@physics.unc.edu

Received 25 January 2009

Published 3 July 2009

Online at stacks.iop.org/JPhysCM/21/296005

Abstract

Magnetic anisotropy, magnetization reversal and the magneto-optic Kerr effect in $\text{Co}_x\text{Mn}_y\text{Ge}_z$ have been studied over a range of compositions between 0 and 50 at.% of Ge and between 1 and 3 in the Co to Mn atomic ratio, including the Heusler alloy Co_2MnGe . A strong quadratic magneto-optic Kerr effect has been observed within a narrow region of composition centered around the Co to Mn atomic ratio of 2, which has been used to probe and quantify the magnetic anisotropy and magnetization reversal of the system. The anisotropy is sixfold with a weak uniaxial component, and it exhibits sensitive dependence on composition, especially on the atomic ratio between Co and Mn. The magnetization reversal process is consistent with the single-domain Stoner–Wohlfarth model.

(Some figures in this article are in colour only in the electronic version)

1. Introduction

Heusler alloys have attracted a lot of attention, owing to their potential for realizing fully spin polarized states at the Fermi level, i.e. half-metal [1–4]. When combined with their crystalline compatibility for epitaxial growth on standard semiconductor substrates, these materials are promising candidates as electronic spin filters for applications in the science and technology of spintronics. In particular the Heusler alloy Co_2MnGe with its high Curie temperature (~ 905 K) and large bulk magnetization ($\sim 5 \mu_B$) is considered as an attractive candidate for the half-metal [5, 6]. However, the highest measured spin polarization reported to date for Co_2MnGe is only about 58% [7], which has been attributed to structural and chemical disorders [8], including the off-stoichiometric

nature of the samples studied. The presence of various defects and/or disorders affects not only the half-metallicity but also the magnetic properties [9], and therefore systematic studies of the properties as a function of composition are of considerable importance. However, these studies are difficult to perform owing to the complexity of a ternary system, and thus most studies of magnetic properties have been limited to single samples with nominal stoichiometric compositions, e.g. Co_2MnGe [10–12]. Recent advances in combinatorial molecular beam epitaxy (MBE) techniques have made it possible to map the composition of an entire ternary system onto a single substrate and to explore the material system systematically [13, 14]. In this paper, we report a systematic and detailed investigation of magnetic anisotropy, magnetization reversal and magneto-optical properties of ternary $\text{Co}_x\text{Mn}_y\text{Ge}_z$ (111) epitaxial films and their correlations with structural properties in a wide range of compositions between 0 and 50 at.% of Ge and between 1 and 3 in the atomic ratio of Co:Mn.

³ Present address: Department of Microelectronics and Applied Physics, Royal Institute of Technology, 164 40 Kista, Sweden.

⁴ Present address: National Synchrotron Light Source II, Brookhaven National Laboratory, Upton, NY 11973, USA.

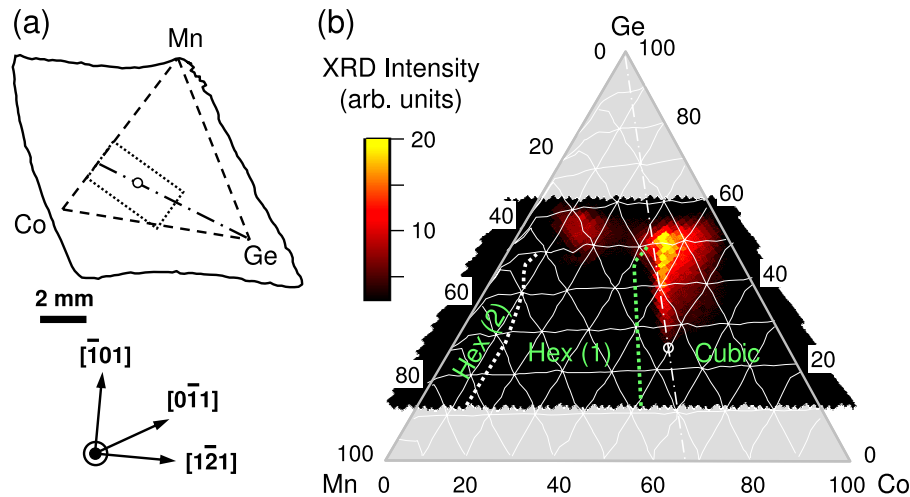


Figure 1. (a) Schematic diagram of the sample showing the outline of the Ge substrate (top) and the crystallographic directions (bottom) with [111] pointing out of the page. The ternary region of composition and the ROI are indicated by the triangle (dashed lines) and the box (dotted lines), respectively. (b) Integrated Bragg intensity and structural phase diagram of the ternary epitaxial film grown on Ge(111). The dotted lines (white and green) separate regions of cubic and two hexagonal phases. The Bragg peaks correspond to (022) reflection for the cubic phase and (012) reflection for the hexagonal phases, and they were integrated along the out-of-plane or surface-normal direction. The contours of composition represent the results of XRF measurements. The dotted-dashed lines and the circles in both (a) and (b) indicate the respective compositional locations for the Co to Mn atomic ratio of 2 and the Heusler stoichiometry, Co_2MnGe .

Magneto-optical properties of Heusler alloys have been studied extensively [15–22], including the observation of a giant Kerr rotation of up to 2.0° at room temperature in PtMnSb [15] and a large second-order magneto-optic Kerr effect (MOKE) in Co_2FeSi [22]. The presence of a second-order or quadratic MOKE (QMOKE) was first shown in a ferromagnet with in-plane magnetization and magnetic field in the plane of incidence of the light [23]. The effect was initially predicted [23] to be small compared to its linear counterpart by up to two orders of magnitude and hence negligible. However, Osgood *et al* [24] reported the observation of strong asymmetries in the hysteresis loops of Fe and Co epitaxial films with in-plane anisotropy. By considering the contribution to the dielectric tensor from the electrons whose equations of motion are not affected by the magnetization, they showed [24] that the observed asymmetries in hysteresis loops indicate the presence of a large QMOKE. However, their analysis of the second-order effect neglects the symmetry of the crystal, which was later determined by Postava *et al* [25, 26] to be essential in order to explain the more complex anisotropic second-order effect observed in Fe films grown on MgO substrates. In this work, composition-dependent evolution of the QMOKE in the ternary epitaxial films of Co, Mn and Ge has been investigated. A very strong QMOKE has been observed within a region of composition, which was used to probe and quantify the magnetic anisotropy and magnetization reversal process of the system. The observed QMOKE is analyzed using a phenomenological model for [111]-oriented films [25, 26], as discussed in section 3. The magnetization reversal process is analyzed using the single-domain Stoner–Wohlfarth model [27].

2. Experiment and structural properties

The ternary composition spread film was grown on a Ge(111) substrate by combinatorial MBE techniques. The

combinatorial synthesis was carried out by sequential deposition of submonolayer ‘wedges’ of each element using shadow masks [13, 14]. The movement of the shadow masks and the associated ‘exposure’ time were controlled in real time using element-specific atomic absorption spectroscopy. Before the growth of the composition spread alloy film, a 200 \AA thick buffer layer of Ge was grown at 350°C and annealed at 650°C , resulting in an atomically smooth Ge surface as determined by *in situ* reflection high energy electron diffraction. The alloy film was grown at 250°C at a deposition rate of 0.1 \AA s^{-1} to a nominal thickness of 630 \AA [28–32], followed by annealing at 450°C for 20 min. These conditions were shown to produce the best structural quality of the Heusler composition [31].

The composition and structural properties of the ternary sample were examined and quantified using microbeam x-ray diffraction (XRD) and x-ray fluorescence (XRF) spectroscopy techniques at the 2-BM beamline of the Advanced Photon Source (APS) at Argonne National Laboratory [32]. Depth-sensitive complementary techniques, including dynamic secondary ion mass spectrometry, electron energy dispersive x-ray spectroscopy and Rutherford backscattering spectroscopy, were also used to quantify the sample composition, especially to separate the Ge content in the film from that in the substrate. A schematic diagram of the combinatorial sample is shown in figure 1(a), indicating the triangular region (dashed line) of the ternary composition spread grown on the Ge(111) substrate and the region of interest (ROI) for this investigation (the dotted rectangle) centered around the Heusler stoichiometry, Co_2MnGe .

A structural phase diagram of the ternary sample, as determined by XRD measurements, is shown in figure 1(b) along with the integrated XRD intensity to illustrate the structural quality of the sample as a function of composition. Above an atomic ratio Co:Mn of $\sim 1.3:1$, the film is cubic. A first-order structural phase transition occurs at this atomic

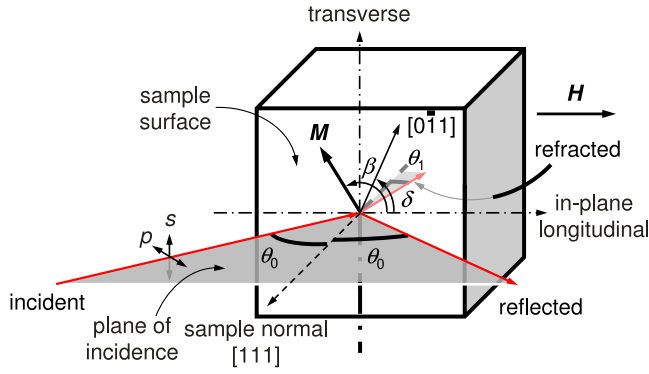


Figure 2. Schematic diagram of the measurements indicating the longitudinal MOKE geometry and the definitions of the parameters.

ratio, below which the film is hexagonal [32]. The integrated XRD intensity corresponds to the (022) Bragg reflection for the cubic phase and the (012) reflection for the hexagonal phases, integrated along the out-of-plane or surface-normal direction. The composition contours in figure 1(b) (and figure 3) correspond to the result of XRF measurements and the nonlinear contours near the Ge-rich side of the Mn–Ge binary alloys are the consequence of Mn surface precipitation and the corresponding depletion of Mn from the film [33].

Within the rectangular ROI, a region with a high degree of structural and chemical ordering is observed, as indicated by the high XRD intensity (figure 1(b)) and the corresponding narrow XRD peak widths for both in-plane and out-of-plane directions (not shown). Below the Ge concentration of ~40 at.%, the highly ordered region is very narrow in composition and centered along the Co to Mn atomic ratio of 2 (the light color region and the dashed–dotted line in figure 1(b), respectively). As the Ge concentration increases above 40 at.%, the region broadens and turns slightly towards a higher Co to Mn atomic ratio. The structural and chemical order of the sample as examined by conventional and anomalous XRD experiments [32, 34] will be reported elsewhere.

The composition-dependent MOKE experiments were carried out systematically within the aforementioned ROI in

a longitudinal geometry with the magnetic field H applied in the film plane and using s-polarized light unless noted otherwise, as shown in figure 2. A stabilized diode laser with a wavelength of 664.3 nm was used and focused to a spot on the sample about 100 μm in diameter, which corresponds to ~1 at.% in the composition space. The signal was modulated using a photoelastic modulator and detected using lock-in techniques for simultaneous detection of the Kerr ellipticity and rotation at once and twice the modulation frequency, respectively. The MOKE signal was normalized with respect to the DC reflectance. The composition dependence was probed by scanning the sample with respect to the laser spot using precision sample positioners. The temperature dependence was measured using a Joule–Thomson refrigerator with a resistive heater. In order to avoid sample degradation and contamination, all measurements were carried out at or below 470 K. Most of the measurements discussed in this paper were done at a constant temperature in field-dependent hysteresis mode versus sample position (thus composition). A typical position-dependent mesh, i.e. hysteresis loops versus position, that covers the ROI with a grid size of 100 μm took 20–30 h to run. Crosshairs with a line width of ~10 μm were scribed on the sample and used to position the various measurements, resulting in a compositional reproducibility of better than 0.2 at.% between different measurements. Magneto-optical properties and magnetic anisotropy within the ROI at room temperature are the main focus of this paper.

3. Theoretical considerations

In this section relevant theoretical considerations for the magneto-optical response in [111]-oriented films are discussed following the approach developed by Postava *et al* [25] in order to facilitate the analysis of MOKE. The magnetization-dependent dielectric tensor, ϵ_{ij} , can be expanded in terms of the direction cosines of magnetization α as

$$\epsilon_{ij}(\alpha) = \epsilon_{ij0} + K_{ijk}\alpha_k + G_{ijkl}\alpha_k\alpha_l + \dots \quad (1)$$

Here, the zeroth-order tensor elements ϵ_{ij0} are independent of magnetization and the direction cosines $\alpha_i \equiv m_i/M_s$

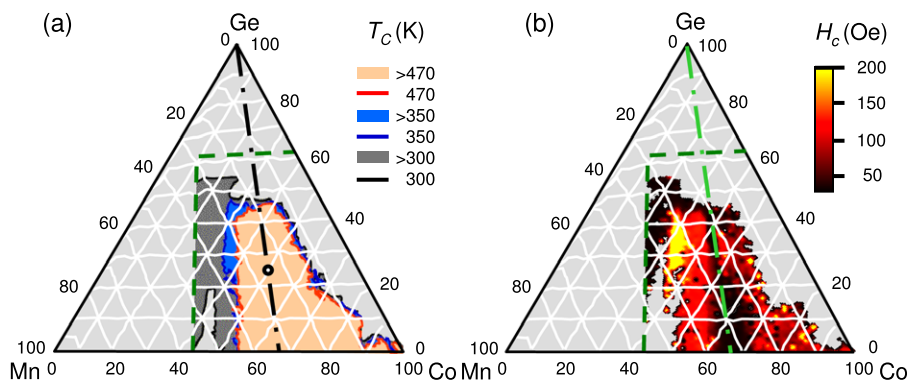


Figure 3. (a) Ferromagnetic regions and Curie temperature (T_c) contours for the ternary alloy around the ROI (to the lower right of the green dashed lines): 300 K (black), 350 K (blue) and 470 K (red). The dotted–dashed line and the circle indicate the respective compositional locations for the Co to Mn atomic ratio of 2 and the Heusler stoichiometry, Co_2MnGe . The ferromagnetic region at 400 K (not shown) is identical to that of 470 K within experimental uncertainty. (b) Map of coercive fields H_c for $H \parallel [121]$ at room temperature. The color scale for H_c has a lower cutoff of 30 Oe, below which it is transparent.

are defined by the i th component of the magnetization m_i and the saturation magnetization M_s . The first- and second-order elements are described by the third rank magneto-optic tensor K_{ijk} and the fourth rank tensor G_{ijkl} , respectively. For magnetic films with cubic symmetry, there is only one unique first-order magneto-optic coefficient, K_{123} , and three quadratic coefficients, G_{1111} , G_{1122} and G_{2323} [35]. By considering the above dielectric tensor up to the second order, the magneto-optical effect for the [111]-oriented films has been calculated using the formalism of You *et al* [36] as discussed in the appendix. The resulting MOKE response, $\phi_{s,p}$, for either s- or p-polarized incident light on a semi-infinite crystal or an optically thick film⁵ is expressed as

$$\phi_{s,p} \approx \mp AK_{123}M_L + \frac{(-\sqrt{2}A \cos 3\delta \mp B)\Delta G \mp 3BG_{2323}}{3} \times M_L M_T + \frac{A \sin 3\delta \Delta G}{3\sqrt{2}}(M_L^2 - M_T^2). \quad (2)$$

Here, M_L and M_T denote the respective longitudinal and transverse components of magnetization with respect to the plane of incidence, as defined by the incident and reflected light (see figure 2). In our case of in-plane magnetic anisotropy, the longitudinal and transverse components are in the sample plane. As shown in figure 2, the magnetic field was applied along the in-plane longitudinal direction, so that M_T vanishes at saturation, and δ is the angle between the in-plane longitudinal direction and the [011] axis of the sample. Based on these definitions, ΔG , the so-called magneto-optical anisotropy parameter, is given by $G_{1111} - G_{1122} - G_{2323}$, which is determined to be different from that of a [001]-oriented system [22, 25, 26]. The constants A and B depend on the optical geometry of the measurement and are given by

$$A = \frac{\cos \theta_0 n_0 n_1 \tan \theta_1}{(n_0 \cos \theta_1 + n_1 \cos \theta_0)(n_0 \cos \theta_0 + n_1 \cos \theta_1)} \quad \text{and} \quad B = \frac{\cos \theta_0 n_0 n_1}{(n_0 \cos \theta_1 + n_1 \cos \theta_0)(n_0 \cos \theta_0 + n_1 \cos \theta_1)}, \quad (3)$$

where θ_0 and θ_1 are the respective angles of incidence and refraction with n_0 and n_1 the respective refractive indices of air (or vacuum) and the film (see figure 2). These four parameters are related to each other through Snell's law.

Equation (2) can be rescaled and expressed in a compact form in terms of the normalized QMOKE coefficients $a_{s,p}(\delta)$ and $b_{s,p}(\delta)$ as

$$\phi_{s,p} \propto \mp M_L + a_{s,p}(\delta)M_L M_T + b_{s,p}(\delta)(M_L^2 - M_T^2) \quad (4)$$

with $a_{s,p}(\delta)$ and $b_{s,p}(\delta)$ given by

$$a_{s,p}(\delta) = \frac{(-\sqrt{2}A \cos 3\delta \mp B)\Delta G \mp 3BG_{2323}}{3AK_{123}}, \quad \text{and} \quad b_{s,p}(\delta) = \frac{\sin 3\delta \Delta G}{3\sqrt{2}K_{123}}. \quad (5)$$

⁵ Films thicker than ~ 500 Å are considered optically thick, where reflections from the film-substrate interface can be neglected; see [37].

In equations (2) and (4) the first term is the linear MOKE (LMOKE), whereas the second and third are the second-order or QMOKE. The coefficients $a_{s,p}(\delta)$ and $b_{s,p}(\delta)$ depend on the higher-order dielectric tensor elements, the polarization of the incident light, the MOKE geometry and the crystallographic symmetry of the sample. The latter dependence on δ (equations (5)) gives rise to optical anisotropy in the second order [26], which exists only in QMOKE and is a consequence of higher-order spin-orbit interactions [24]. In general, if the fourth rank tensor elements are not negligible when compared to that of the third rank tensor (e.g. K_{123}) as a result of spin-orbit interactions [24, 25], QMOKE becomes detectable.

In the absence of QMOKE, MOKE hysteresis loops possess the inversion symmetry of M_L . In contrast, QMOKE as a function of H has a reflection symmetry with respect to $H = 0$, owing to its dependence on M_T . When it becomes significant, the perfect inversion symmetry is destroyed and the transverse component of the magnetization M_T becomes detectable in the hysteresis loops. The MOKE response thus contains a mixture of two symmetry components, one with inversion symmetry (LMOKE) and another with reflection symmetry (QMOKE), such that $\text{LMOKE}(H_{\uparrow\downarrow}) = -\text{LMOKE}(-H_{\uparrow\downarrow})$ and $\text{QMOKE}(H_{\uparrow\downarrow}) = \text{QMOKE}(-H_{\uparrow\downarrow})$ with the subscript arrows indicating the sweep directions of H . Therefore, LMOKE and QMOKE can be obtained from the MOKE response $\phi(H_{\uparrow\downarrow})$ and its reflection conjugate $\phi'(H_{\uparrow\downarrow}) [= \phi(-H_{\uparrow\downarrow})]$ using the following symmetry operations [22]:

$$\begin{aligned} \text{LMOKE}(H_{\uparrow\downarrow}) &= [\phi(H_{\uparrow\downarrow}) - \phi'(H_{\uparrow\downarrow})]/2 \quad \text{and} \\ \text{QMOKE}(H_{\uparrow\downarrow}) &= [\phi(H_{\uparrow\downarrow}) + \phi'(H_{\uparrow\downarrow})]/2. \end{aligned} \quad (6)$$

4. Results and discussion

Magnetism of the ternary $\text{Co}_x\text{Mn}_y\text{Ge}_z(111)$ epitaxial film has been examined by MOKE as a function of composition at various temperatures. Compositional regions with finite saturation MOKE responses and coercive fields (H_c) are identified as ferromagnetic, while those with linear field dependence are paramagnetic. The boundary between the two regions is approximately the contour of the Curie temperature T_C . The ferromagnetic regions and the corresponding T_C contours at several temperatures are shown in figure 3(a). A region of high T_C (>470 K) exists within the ROI and the nearly identical ferromagnetic regions between 350 and 470 K indicate a sharp rise in T_C at their boundaries. As shown in figure 3(b), the room temperature coercivity exhibits low values within a narrow region of composition centered around the Co to Mn atomic ratio of 2 (the dark color region and the dotted-dashed line). These magnetic behaviors (figure 3) appear to correlate with the structural properties of the film (figure 1(b)). Specifically, the boundary of the high temperature ferromagnetic region near the Co to Mn atomic ratio of 1.3 (the left boundary of the 470 K region in red in figure 3(a)) and the corresponding sharp rise in T_C appear to coincide with the composition, where the first-order structural phase transition from hexagonal to cubic takes place (the green

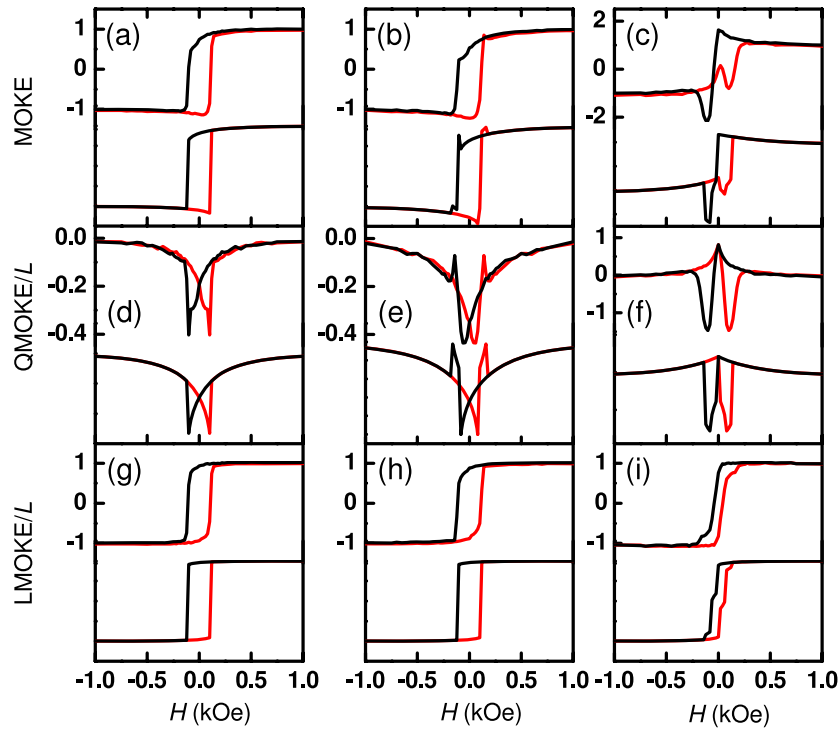


Figure 4. MOKE (top row), QMOKE, (middle row) and LMOKE (bottom row) hysteresis loops at Co:Mn = 2 and various Ge concentrations: 15 at.% Ge (left column), 25 at.% Ge (middle column) and 45 at.% Ge (right column). The magnetic field for these loops was applied at $\delta = 75^\circ$ measured from [011] and the incident laser light was s-polarized with the angle of incidence of about 10° . The measured hysteresis loops are shown above the calculated loops. The parameters used for the model calculations are $K_6/M_s = 1000$ Oe, $K_u/M_s = 0$ Oe, $a = -0.3$ and $b = 0.5$ for the left column, $K_6/M_s = 1200$ Oe, $K_u/M_s = 24$ Oe, $a = -0.5$ and $b = 0.5$ for the middle column, and $K_6/M_s = 800$ Oe, $K_u/M_s = 40$ Oe, $a = 2.0$ and $b = 0.5$ for the right column. The black and red lines correspond to H_\downarrow and H_\uparrow , respectively.

dotted line in figure 1(b)). In addition, the narrow region of low coercivity along Co:Mn = 2 (figure 3(b)) also appears to coincide with that of high crystalline perfection (the high intensity region in figure 1(b)). These correlations suggest that the magnetic phenomena are composition driven.

Room temperature MOKE hysteresis loops within the ROI exhibit ‘asymmetric’ features, including ‘spikes’ and ‘dips’, as shown in figures 4(a)–(c) for several compositions. For opposite field sweep directions ($H_{\downarrow/\uparrow}$) the MOKE loops are different, such that they do not exhibit inversion symmetry. As discussed above, the deviation from perfect inversion symmetry in the hysteresis loops is a distinguishing feature for the presence of QMOKE and it also provides a measure for the strength of QMOKE. The examples shown in figures 4(a)–(c) indicate that the QMOKE becomes stronger as the Ge concentration increases.

QMOKE and LMOKE signals have been separated using the symmetry operations given by equation (6) and normalized by the saturation value of LMOKE (L), as shown in figures 4(d)–(i) for the three examples. The QMOKE loops are very sensitive to the composition, exhibiting different features at different Ge concentrations. In the three examples shown, the largest amplitude of normalized QMOKE is about 2.5 (figure 4(f)), which is the largest value we are aware of in the literature, evidently a result of very strong higher-order spin–orbit interactions [24, 25]. The LMOKE loops, on

the other hand, are symmetrical about the origin, exhibiting the usual inversion symmetry. For a constant Co to Mn atomic ratio of 2, their shapes do not change much for Ge concentration below ~ 40 at.% (figures 4(g) and (h)), but at higher Ge concentrations, steps appear in the hysteresis loops that are consistent with a two-step switching of magnetization (figure 4(i)).

The dependence of QMOKE as a function of composition has been examined systematically. For a fixed Ge concentration, QMOKE is suppressed for Co:Mn of less than 1.3, and it generally exhibits the largest amplitudes around Co:Mn of 2, as shown in figure 5(a) for 25 at.% Ge. For instance, the amplitudes for Co:Mn of 2.1 and 2.2 are larger than those at Co:Mn of <1.7 and >3 (figure 5(a)). The counterparts for a constant Co:Mn of 2 are very large, as shown in figure 5(b). While the QMOKE amplitudes depend on the angle of incidence and the direction of H (δ), the composition-dependent trend is qualitatively represented in figures 5(a) and (b), such that the largest values of QMOKE amplitudes exhibit a ridge along the composition with Co:Mn = 2 [38]. Like the other magnetic properties described above, the behavior of QMOKE amplitudes also correlates with structural properties, e.g. coincidence of regions of large QMOKE values and high crystalline quality (figure 1) [34]. The QMOKE values near the Heusler stoichiometry Co_2MnGe are comparable to previously reported values for Heusler alloys of PtMnSb [16] and Co_2FeSi [22].

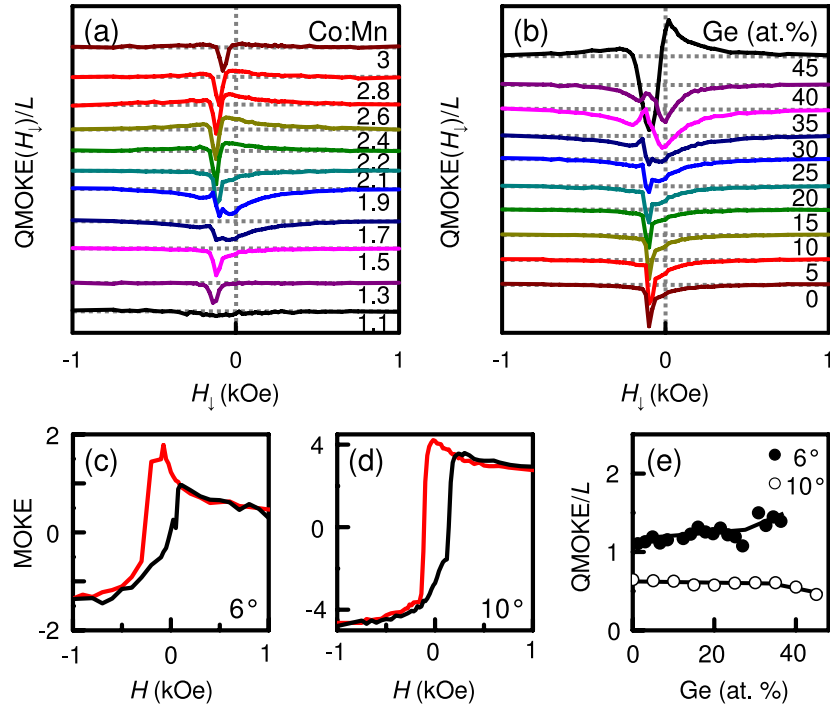


Figure 5. Normalized QMOKE signal versus H_{\perp} as a function of composition for $\delta = 75^{\circ}$ and an angle of incidence of 10° : (a) dependence on Co:Mn at a fixed Ge concentration of 25 at.% and (b) dependence on Ge concentration at a fixed Co:Mn of 2. Examples of hysteresis loops for Co_2MnGe at two angles of incidence: (c) $\theta_0 = 6^{\circ}$ and (d) $\theta_0 = 10^{\circ}$. (e) Dependence of QMOKE/L amplitude on Ge concentration at Co:Mn = 2 for two different angles of incidence and $\delta = -30^{\circ}$.

Dependence of MOKE on incident angle of the laser has also been examined. As shown in figures 5(c) and (d) for Co_2MnGe for two incident angles, the saturation MOKE intensity and thus saturation LMOKE increase with increasing incident angle from $\theta_0 = 6^{\circ}$ to 10° , whereas the amplitude of QMOKE decreases slightly. This trend is generally preserved at other Ge concentrations with Co:Mn = 2, as shown in figure 5(e). The observed dependence on incident angle is consistent with the model discussed in section 3. Specifically, the pre-factor of LMOKE (equation (2)) is proportional to the geometric factor A (equations (3)) that vanishes as the incident angle approaches 0° , resulting in a suppression of LMOKE. In contrast, QMOKE depends on both A and B (equations (2) and (3)), and as the angle of incidence decreases towards 0° , B increases and thus the QMOKE contribution from $M_L M_T$ would increase correspondingly, while the contribution from $M_L^2 - M_T^2$ would vanish. This finding is in agreement with the literature [24, 25].

As discussed in section 3 (equations (2) and (4)), the strong QMOKE enhances the sensitivity for detecting and quantifying magnetization directions, since both M_L and M_T are detectable. We note that, even in the absence of QMOKE, both in-plane and out-of-plane components of the magnetization can be detected by separate MOKE measurements involving the rotation of the optics with respect to the plane of incidence [39]. In our case both M_L and M_T are obtained in a single measurement due to the large QMOKE observed in these films, which has been used to study magnetic anisotropy and magnetization reversal of the system as a function of composition. MOKE hysteresis loops for a

field applied along various in-plane directions (more than 10) have been measured and analyzed, including all in-plane (110) and (112) directions, as shown in figures 6 and 7 for several sets of characteristic results versus composition. The behaviors for Co:Mn = 2 at various Ge concentrations are shown in figure 6 and those for a constant Ge concentration at different atomic ratios between Co and Mn are shown in figure 7, and they are described as follows.

At a constant Co to Mn atomic ratio of 2 (figure 6), the MOKE hysteresis loops generally exhibit inversion asymmetry which is characterized by asymmetric ‘dips’ and ‘spikes’. The asymmetry increases monotonically with increasing Ge concentration (from figures 6(a)–(c)), leading to hysteresis loops with unusual double spikes near coercive fields (figure 6(c)). These features indicate not only the presence of strong QMOKE but also the existence of coherent rotation during magnetization reversal [24], since the asymmetric features themselves are the result of the transverse component of the magnetization, as discussed above (equations (2) and (4)). A lack of coherent rotation would evidently give rise to cancellations of the transverse components. For a given composition, the hysteresis loops reverse the asymmetry with respect to two in-plane axes, where the hysteresis loops are nearly ‘square’. For instance, the two axes are approximately along $[0\bar{1}1]$ and $[\bar{2}11]$ for 15 at.% of Ge (arrows in figure 6(a)), and for 45 at.% of Ge (arrows in figure 6(c)) one axis appears to be in between $[\bar{1}21]$ and $[0\bar{1}1]$ and another in between $[\bar{1}01]$ and $[\bar{2}11]$. The behavior is generally associated with the presence of uniaxial magnetic anisotropy (UMA). However, the threefold crystallographic symmetry would give

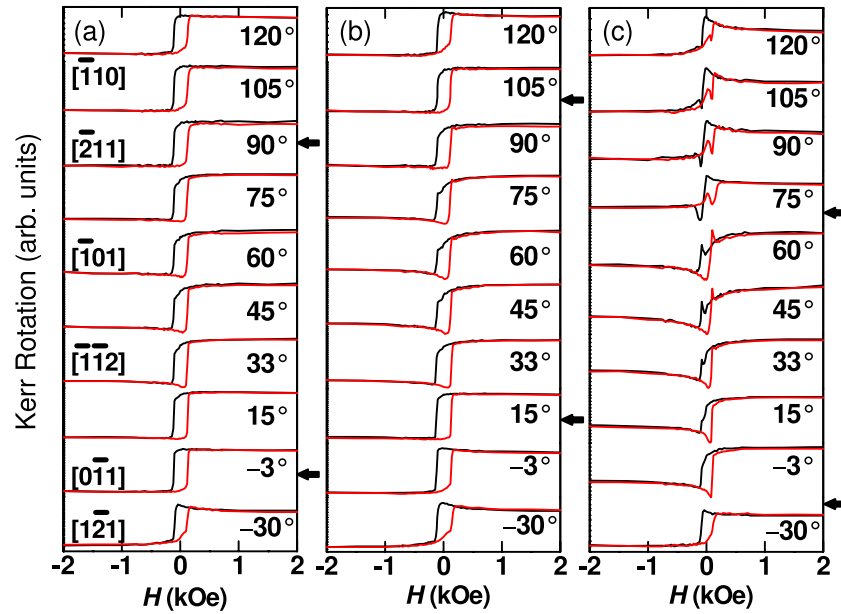


Figure 6. Hysteresis loops versus field orientation at various Ge concentrations for $\text{Co}_x\text{Mn}_y\text{Ge}_z$ at Co:Mn ($x:y$) = 2: (a) $z = 15$, (b) $z = 25$ and (c) $z = 45$ at.% Ge. Arrows indicate the orientations where hysteresis loops reverse the asymmetry.

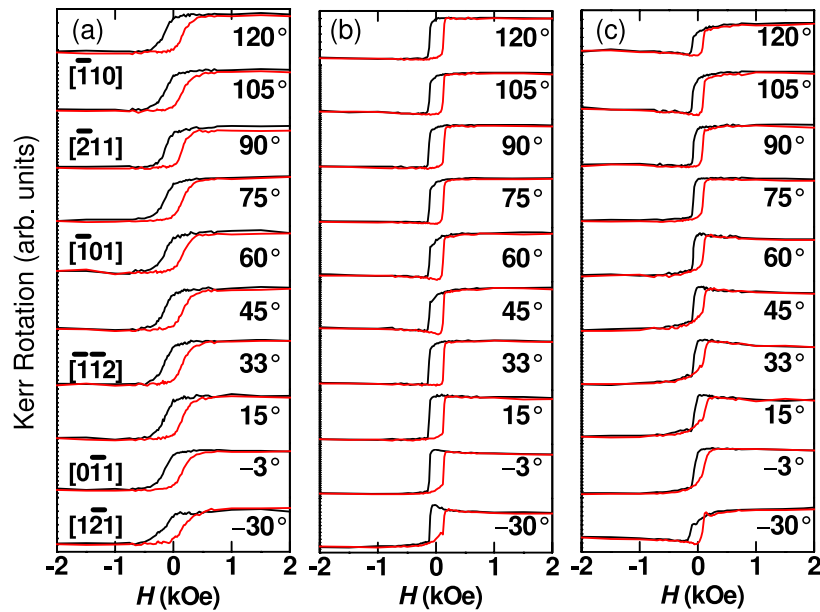


Figure 7. Hysteresis loops versus field orientation at several Co to Mn atomic ratios for $\text{Co}_x\text{Mn}_y\text{Ge}_z$ at $z = 25$ at.% Ge: (a) $x:y = 1$, (b) $x:y = 2$ and (c) $x:y = 3$.

rise to sixfold magnetic anisotropy. The rather complex angle-dependent hysteresis loops suggest that there are two anisotropy components. The presence of such complexity would require the hysteresis loops be modeled and calculated in order to analyze and quantify the magnetic anisotropy of the system and the magnetization reversal process.

At compositions away from the Co to Mn atomic ratio of 2, the hysteresis loops are significantly different (figure 7). For an atomic ratio of less than 1.5 between Co and Mn, MOKE hysteresis loops are identical in all directions with an increased switching width (figure 7(a) for an atomic ratio Co:Mn of 1), indicating the absence of magnetic anisotropy

in this range of composition. The observed transition from anisotropy to isotropy around an atomic ratio Co:Mn of 1.5 appears to correlate with the first-order structural phase transition from cubic to hexagonal (figure 1(b)) [32]. In contrast, when the Co to Mn atomic ratio becomes greater than 2, an inversion in the hysteresis asymmetry takes place, as shown in figures 7(b) and (c). The behavior indicates a change in magnetic anisotropy.

The complex hysteresis loops have been analyzed using the free energy for magnetic anisotropy and the Stoner–Wohlfarth (SW) model [27] of single-domain magnetization reversal [40–43]. The free energy density of a single domain

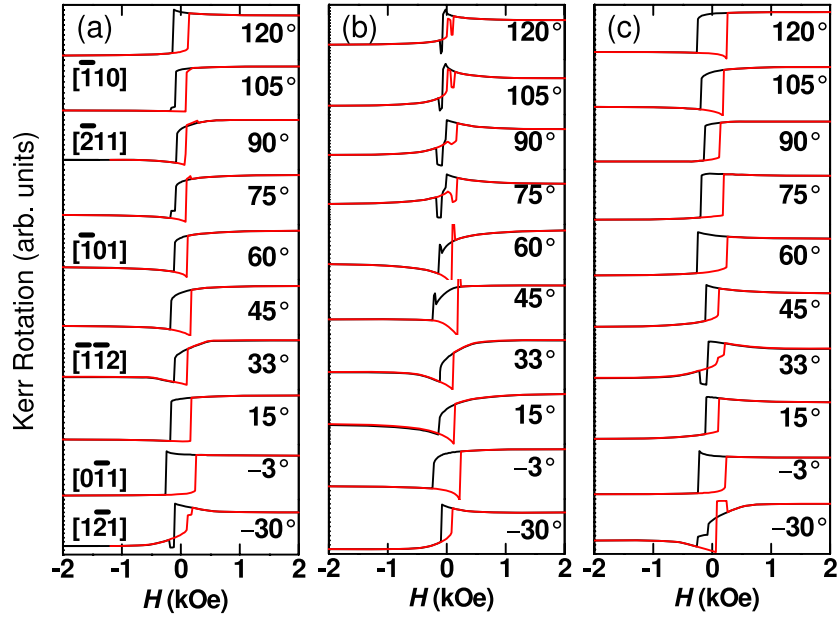


Figure 8. Calculated hysteresis loops versus magnetic field orientation for $\text{Co}_x\text{Mn}_y\text{Ge}_z$ at (a) $z = 25$ at.% Ge and $x:y = 2$, (b) $z = 45$ at.% Ge and $x:y = 2$, and (c) $z = 25$ at.% Ge and $x:y = 3$. The parameters used for the model calculation are $K_6/M_s = 1000$ Oe, $K_u/M_s = 0$ Oe for (a), $K_6/M_s = 1200$ Oe, $K_u/M_s = 24$ Oe for (b), and $K_6/M_s = 1200$ Oe, $K_u/M_s = -24$ Oe for (c). The error in K_6/M_s is about 100 Oe, whereas the error in K_u/M_s is about 3 Oe. As indicated in the text, the values of a and b change with orientation.

of magnetization M in a magnetic field H for a cubic crystal can be expressed as [40–43]

$$E = K_4(\alpha_1^2\alpha_2^2 + \alpha_1^2\alpha_3^2 + \alpha_2^2\alpha_3^2) + K_6\alpha_1^2\alpha_2^2\alpha_3^2 - M \cdot H, \quad (7)$$

where K_4 and K_6 are the first two cubic anisotropy constants. The direction cosines of M are defined with respect to the cubic crystal axes. The last term represents the Zeeman energy. The demagnetization energy is neglected here, owing to thin-film geometry with in-plane magnetic field. For (111) in-plane magnetic anisotropy, only the sixfold magnetic anisotropy (the term associated with (111) crystalline symmetry, K_6) remains, whereas the term involving K_4 vanishes. As mentioned above for the angle-dependent hysteresis loops, it maybe necessary to include a UMA component in the in-plane magnetic anisotropy, and thus the corresponding free energy E_{IPMA} is given by

$$E_{\text{IPMA}} = K_6(28 - \cos 6\theta_M)/108 + K_u \sin^2(\theta_M - \varphi) - M_s H \cos(\delta - \theta_M), \quad (8)$$

where θ_M is the angle between M and one of the sixfold easy axes (for $K_6 > 0$), and K_u is the UMA constant with φ being the angle between the uniaxial easy axis and one of the sixfold easy axes. The first and third terms in equation (8) are derived from equation (7).

In the SW model the magnetic anisotropy energy E_{IPMA} (i.e. its local minimum) and the history of H determine the direction of M . At high fields (above saturation), M lies in a global minimum of E_{IPMA} and, as the field decreases, the energy minimum shifts so M rotates to follow the locus of the minimum. When this minimum vanishes, M would jump to a new neighboring minimum. Therefore, it is possible to calculate M from the local minimum of the free energy

(equation (8)) and thus the MOKE hysteresis loops using equation (4), and in turn to assess whether the measured magnetization reversal (figures 4–7) is consistent with the SW model. The calculation has been carried out treating K_6/M_s , K_u/M_s , $a_{s,p}(\delta)$ and $b_{s,p}(\delta)$ as the adjustable parameters. The results are shown in figures 4 and 8 and they demonstrate good qualitative agreement with the corresponding measurements shown in figures 4, 6 and 7. By reproducing the asymmetry and the spikes, the comparisons illustrate that the magnetization reversal process in this system is indeed consistent with the SW model. The differences in coercive fields at some angles can be attributed to effects that are not taken into account in the SW model [41], including those associated with micromagnetic effects and defects. For all compositions, the sixfold easy axes are found to be along the in-plane $\langle 110 \rangle$ directions consistent with the crystal symmetry. A weak UMA is often necessary to produce the distinct features in the hysteresis loops and, for instance, near the Heusler stoichiometry, the UMA easy axis is near $\langle 0\bar{1}1 \rangle$. While there are various extrinsic sources and interactions that affect the nature and strength of magnetic anisotropy, the observed composition dependence, particularly its sensitivity on the Co to Mn atomic ratio, strongly supports the presence of an intrinsic composition-driven phenomenon.

In most cases a unique set of K_6/M_s , K_u/M_s , $a_{s,p}(\delta)$ and $b_{s,p}(\delta)$ has been obtained that reproduces the experimental behavior for a given composition, but the values for $a_{s,p}(\delta)$ and $b_{s,p}(\delta)$ must vary as a function δ (see figure 2) suggesting the presence of anisotropy in QMOKE. However, attempts to confirm this anisotropy (equations (5)) were unsuccessful, owing primarily to the longitudinal MOKE geometry where M_T is often very small and vanishes at saturation. Only a small fraction of hysteresis loops that contain sufficiently large M_T

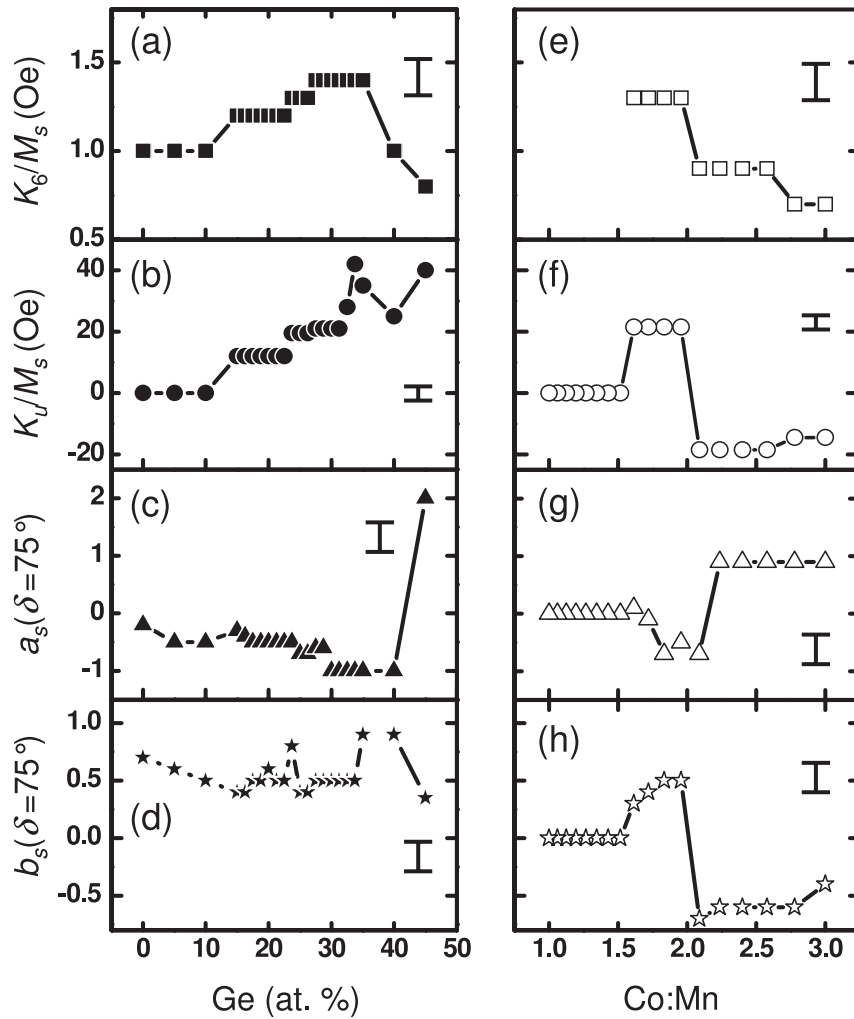


Figure 9. Evolution of magnetic anisotropy constants and QMOKE parameters as a function of composition: left column ((a)–(d) from top to bottom), dependence on Ge concentration at a Co to Mn atomic ratio of 2, right column ((e)–(h) from top to bottom), dependence on Co:Mn at 25 at.% Ge. The error bars are shown on the right of each plot.

would yield reliable values of $a_{s,p}(\delta)$ and $b_{s,p}(\delta)$, particularly for loops near magnetic hard axes (e.g. between $[211]$ and $[\bar{1}01]$ or $\delta = 75^\circ$). For most field directions, the analysis has produced values with large uncertainties that contain too much scattering to make an adequate comparison with the δ dependence given by equations (5). In contrast, the magnetic anisotropy constants (K_6/M_s and K_u/M_s) from the analysis stay the same and are thus independent of δ .

Composition-dependent evolution of magnetic anisotropy constants and QMOKE coefficients has been examined, as shown in figure 9. For a constant Co to Mn atomic ratio of 2 (the left column in figure 9, i.e. (a) to (d) from top to bottom), the sixfold anisotropy constant K_6/M_s exhibits a broad peak at ~ 30 at.% of Ge (figure 9(a)), while the UMA counterpart K_u/M_s with its easy axis near $\langle 011 \rangle$ exhibits nearly a monotonic increase with Ge concentration (figure 9(b)). The constants near the Heusler stoichiometry are $K_6/M_s = (1200 \pm 100)$ Oe and $K_u/M_s = (20 \pm 3)$ Oe. Using the saturation magnetic moment of 1200 ± 200 emu cm^{-3} for a similar film [30], which is comparable to the bulk value [6] of 1000 emu cm^{-3} , K_6 is about $(1.0 \pm 0.2) \times 10^6$ ergs cm^{-3} .

This value is one order of magnitude larger than that for $[111]$ -oriented Fe films [44, 45]. The UMA constant is comparable to that of Co_2MnGe (001) films reported in the literature [10, 12]. For a constant angle δ , the magnitude of the coefficient $a_{s,p}$ is generally larger than the coefficient $b_{s,p}$, as shown in figures 9(c) and (d), respectively. While the latter is nearly constant, $a_{s,p}$ decreases with increasing Ge concentration up to about 45 at.%, where a sign change takes place accompanied by a sharp increase to about 2.

The behaviors for both anisotropy and QMOKE parameters exhibit sharp transitions versus the atomic ratio between Co and Mn (Co:Mn), as shown in the right-hand column of figure 9 (i.e. (e)–(h) from top to bottom) for a constant Ge concentration of 25 at.%. The absolute values of all the parameters are the largest near a Co:Mn of 2, indicating that the strongest magnetic anisotropies and QMOKE values correlate with the highest degree of structural and chemical ordering. Below a Co:Mn of 1.5, all parameters vanish sharply, corresponding to vanishing magnetic anisotropy and QMOKE. As mentioned above, the sharp transition correlates with a first-order structural phase transition from cubic to hexagonal. In contrast, the parameters (except K_6) exhibit a sharp change of

sign right above a Co:Mn of 2 which does not appear to correlate with any structural transition. Here, a change of sign in the UMA corresponds to a 90° rotation of the easy axis from near $\langle 0\bar{1}1 \rangle$ to near $\langle 01\bar{1} \rangle$.

Both magnetic anisotropy and QMOKE depend on spin-orbit interactions that are very sensitive to the structural and chemical symmetry of the system. Our conventional and anomalous x-ray diffraction experiments and analysis (to be reported elsewhere) indicate a significant increase in site swapping and thus reduction in chemical order above a Co:Mn of 2. A sharp change in anisotropy and a sign change in QMOKE parameters appear to be the result of such a change in the local chemical environment of the system, thus giving rise to a corresponding change in the spin-orbit interactions.

5. Summary

The magneto-optical effect, magnetic anisotropy and magnetization reversal process of (111) epitaxial films of $\text{Co}_x\text{Mn}_y\text{Ge}_z$ ternary alloys have been studied over a large range of compositions, including the Heusler alloy Co_2MnGe . Within a narrow region of compositions centered around the Co to Mn atomic ratio of 2, a very strong QMOKE has been observed, which appears to correlate with structural and chemical ordering of the system. A model for the QMOKE has been developed and discussed in order to elucidate the asymmetric hysteresis loops and to probe and quantify the magnetic properties of the system. The magnetization reversal process is shown to be in good qualitative agreement with the Stoner–Wohlfarth model of single-domain magnetization reversal. The magnetic anisotropy is sixfold with a weak uniaxial component, and it also exhibits sensitive dependence on the atomic ratio between Co and Mn. These findings suggest that the presence of a composition-driven structural and chemical ordering may be responsible for the observed magnetism and magneto-optical properties.

Acknowledgments

The work is supported by US DOE BES DE-FG02-05ER46216. MBE synthesis is supported by US NSF DMR-0441218. Use of the Advanced Photon Source is supported by the US Department of Energy, Office of Sciences, Office of Basic Energy Sciences, under contract no. DE-AC02-06CH11357. An APS subcontract no. 5F-00428 for partial student support (BAC) is also acknowledged.

Appendix. Derivation of magneto-optic Kerr effect up to second order for [111]-oriented films

For cubic crystals, the dielectric tensor elements in equation (1) (section 3) can be written as [35, 46]

$$\begin{aligned}\epsilon_{11} &= G_{1111}\alpha_1^2 + G_{1122}\alpha_2^2 + G_{1122}\alpha_3^2 + \epsilon_{xx0} \\ \epsilon_{12} &= G_{2323}\alpha_1\alpha_2 - K_{123}\alpha_3 \\ \epsilon_{13} &= K_{123}\alpha_2 + G_{2323}\alpha_1\alpha_3 \\ \epsilon_{21} &= G_{2323}\alpha_1\alpha_2 + K_{123}\alpha_3\end{aligned}$$

$$\begin{aligned}\epsilon_{22} &= G_{1122}\alpha_1^2 + G_{1122}\alpha_2^2 + G_{1122}\alpha_3^2 + \epsilon_{xx0} \\ \epsilon_{23} &= G_{2323}\alpha_2\alpha_3 - K_{123}\alpha_1 \\ \epsilon_{31} &= -K_{123}\alpha_2 + G_{2323}\alpha_1\alpha_3 \\ \epsilon_{32} &= G_{2323}\alpha_2\alpha_3 + K_{123}\alpha_1 \\ \epsilon_{33} &= G_{1122}\alpha_1^2 + G_{1122}\alpha_2^2 + G_{1111}\alpha_3^2 + \epsilon_{xx0}.\end{aligned}\tag{A.1}$$

Here, the direction cosines for the magnetization α_1 , α_2 and α_3 are defined with respect to the cubic axes [100], [010] and [001], respectively. As shown in equations (A.1), each of the off-diagonal elements has a linear and a quadratic magnetization-dependent term, while the dependence for the diagonal terms is exclusively quadratic. In order to transform the dielectric tensor ϵ_{ij} from the cubic basis to the frame of reference for the measurements, i.e. [111] orientation $\epsilon_{ij}^{(111)}$, an orthogonal transformation matrix l has been used:

$$l = \begin{pmatrix} -\sqrt{\frac{2}{3}}\sin\delta & \frac{\sin\delta}{\sqrt{6}} - \frac{\cos\delta}{\sqrt{2}} & \frac{\cos\delta}{\sqrt{2}} + \frac{\sin\delta}{\sqrt{6}} \\ -\sqrt{\frac{2}{3}}\cos\delta & \frac{\sin\delta}{\sqrt{6}} + \frac{\cos\delta}{\sqrt{2}} & -\frac{\sin\delta}{\sqrt{6}} + \frac{\cos\delta}{\sqrt{2}} \\ \frac{1}{\sqrt{3}} & \frac{1}{\sqrt{3}} & \frac{1}{\sqrt{3}} \end{pmatrix},\tag{A.2}$$

where δ is the angle between the in-plane longitudinal direction and the $[0\bar{1}1]$ axis of the sample (see figure 2).

For a second rank tensor, the transformation is given by (Neumann's principle) [35]

$$\epsilon_{ij}^{(111)} = l_{im}l_{jn}\epsilon_{mn}.\tag{A.3}$$

The MOKE signal is calculated from using the magneto-optical Fresnel reflection matrix given by

$$\mathbf{R} = \begin{pmatrix} r_{pp} & r_{ps} \\ r_{sp} & r_{ss} \end{pmatrix},\tag{A.4}$$

where r_{ij} elements correspond to the ratios between the incident j polarized electric field and the reflected i polarized electric field. The explicit expressions for r_{ij} for a semi-infinite or optically thick film (see footnote 3) are [23, 36, 47]

$$\begin{aligned}r_{pp} &= \frac{\cos\theta_0 n_1 - \cos\theta_1 n_0}{\cos\theta_0 n_1 + \cos\theta_1 n_0} + \frac{2\cos\theta_0 \sin\theta_1 n_1 n_0 \epsilon_{32}^{(111)}}{\cos\theta_0 n_1 + \cos\theta_1 n_0}, \\ r_{sp} &= \frac{-\cos\theta_0 n_1 n_0 \epsilon_{13}^{(111)} \tan\theta_1 + \cos\theta_0 n_1 n_0 \epsilon_{12}^{(111)}}{(\cos\theta_0 n_1 + \cos\theta_1 n_0)(\cos\theta_0 n_0 + \cos\theta_1 n_1)}, \\ r_{ps} &= -\frac{\cos\theta_0 n_1 n_0 \epsilon_{31}^{(111)} \tan\theta_1 + \cos\theta_0 n_1 n_0 \epsilon_{21}^{(111)}}{(\cos\theta_0 n_1 + \cos\theta_1 n_0)(\cos\theta_0 n_0 + \cos\theta_1 n_1)}, \\ r_{ss} &= \frac{\cos\theta_0 n_1 - \cos\theta_1 n_0}{\cos\theta_0 n_0 + \cos\theta_1 n_1},\end{aligned}\tag{A.5}$$

where θ_0 and θ_1 are the respective angles of incidence and refraction with n_0 and n_1 the respective refractive indices of air (or vacuum) and the film. The parameters are related to each other through Snell's law. In equations (A.5), higher-order terms of the type $\epsilon_{ij\epsilon_{kl}}$ and reflections from the film-substrate interface are neglected (see footnote 3). Finally, Kerr effects for s- and p-polarized light are given by the relation

$$\phi_s = r_{ps}/r_{ss} \quad \phi_p = r_{sp}/r_{pp}.\tag{A.6}$$

The MOKE response up to the second order as given by equation (2) has been derived by first calculating the direction cosines of the magnetization for the [111] orientation. As shown in figure 2, the magnetization M is assumed to be in the film plane, and the angle between M and the in-plane longitudinal axis is β , such that $M_L = \cos \beta$ and $M_T = \sin \beta$. The direction cosines of the magnetization can then be expressed in terms of M_L and M_T :

$$\begin{aligned}\alpha_1 &= -\sqrt{2/3} \cos(\delta - \beta) \\ \alpha_2 &= (1/\sqrt{6}) \cos(\delta - \beta) + (1/\sqrt{2}) \sin(\delta - \beta), \\ \alpha_3 &= (1/\sqrt{6}) \cos(\delta - \beta) - (1/\sqrt{2}) \sin(\delta - \beta).\end{aligned}\quad (\text{A.7})$$

These direction cosines can now be substituted into equations (A.1) and then transformed to the dielectric tensor elements for the [111] orientation using equation (A.3). Finally, the MOKE response (equation (2) in section 3) can be obtained from the Fresnel reflection matrix (equations (A.4) and (A.5)) and equations (A.6).

References

- [1] Pickett W E and Moodera J S 2001 *Phys. Today* **54** 39
- [2] de Groot R A, Mueller F M, van Engen P G and Buschow K H J 1983 *Phys. Rev. Lett.* **50** 2024
- [3] Irkhin V Y and Katsnel'son M I 1994 *Phys.—Usp.* **37** 659
- [4] Fujii S, Ishida S and Asano S 1994 *J. Phys. Soc. Japan* **63** 1881
- [5] Ishida S, Masaki T, Fujii S and Asano S 1998 *Physica B* **245** 1
- [6] Webster P J and Ziebeck K R A 1988 *Landolt–Börnstein-Group III Condensed Matter* vol 19c, ed P J Webster and K R A Ziebeck (Berlin: Springer) pp 75–9
Webster P J 1971 *J. Phys. Chem. Solids* **32** 1221
- [7] Rajanikanth A, Takahashi Y K and Hono K 2007 *J. Appl. Phys.* **101** 023901
- [8] Ravel B, Cross J O, Raphael M P, Harris V G, Ramesh R and Saraf V 2002 *Appl. Phys. Lett.* **81** 2812
- [9] Picozzi S, Continenza A and Freeman A J 2004 *Phys. Rev. B* **69** 094423
- [10] Ambrose T, Krebs J J and Prinz G A 2000 *Appl. Phys. Lett.* **76** 3280
- [11] Yang F Y, Shang C H, Chien C L, Ambrose T, Krebs J J, Prinz G A, Nikitenko V I, Gornakov V S, Shapiro A J and Shull R D 2002 *Phys. Rev. B* **65** 174410
- [12] Westerholt K, Bergmann A, Grabis J, Nefedov A and Zabel H 2005 *Half-Metallic Alloys: Fundamentals and Applications (Springer Lecture Notes in Physics* vol 676) (Berlin: Springer) p 67
- [13] Yoo Y K and Tsui F 2002 *MRS Bull.* **27** 316
- [14] Tsui F and He L 2005 *Rev. Sci. Instrum.* **76** 062206
- [15] Van Engen P G, Buschow K H J, Jongeureur R and Erman M 1983 *Appl. Phys. Lett.* **42** 202
- [16] Carey R, Newman D M and Wears M L 1998 *Phys. Rev. B* **58** 14175
- [17] Antonov V N, Yaresko A N, Perlov A Ya, Nemoshkalenko V V, Oppeneer P M and Eschrig H 1999 *Low Temp. Phys.* **25** 387
- [18] Miyamoto K, Kimura A, Iori K, Sakamoto K, Xie T, Moko T, Qiao S, Taniguchi M and Tsuchiya K 2004 *J. Phys.: Condens. Matter* **16** S5797
- [19] Nefedov A, Grabis J, Bergmann A, Westerholt K and Zabel H 2004 *Physica B* **345** 250
- [20] Grabis J, Bergmann A, Nefedov A, Westerholt K and Zabel H 2005 *Phys. Rev. B* **72** 024437
- [21] Ricci F, Picozzi S, Continenza A, D'Orazio F, Lucari F, Westerholt K, Kim M and Freeman A J 2007 *Phys. Rev. B* **76** 014425
- [22] Hamrle J, Blomeier S, Gaier O, Hillebrands B, Schneider H, Jakob G, Postava K and Felser C 2007 *J. Phys. D: Appl. Phys.* **40** 1563
- [23] Metzger G, Pluvinaige P and Torguet P 1965 *Ann. Phys., Paris* **10** 5
- [24] Osgood R M III, Clemens B M and White R L 1997 *Phys. Rev. B* **55** 8990
Osgood R M III, Bader S D, Clemens B M, White R L and Matsuyama H 1998 *J. Magn. Magn. Mater.* **182** 297
- [25] Postava K, Jaffres H, Schuhl A, Nguyen Van Dau F, Goiran M and Fert A R 1997 *J. Magn. Magn. Mater.* **172** 199
- [26] Postava K, Hrabovský D, Pištora J, Fert A R, Višňovský Š and Yamaguchi T 2002 *J. Appl. Phys.* **91** 7293
- [27] Stoner E C and Wohlfarth E P 1948 *Phil. Trans. R. Soc. A* **240** 74
- [28] Vogt S, Chu Y S, Tkachuk A, Ilinski P, Walko D A and Tsui F 2004 *Appl. Surf. Sci.* **223** 214
- [29] Chu Y S, Tkachuk A, Vogt S, Ilinski P, Walko D A, Mancini D C, Dufresne E M, He L and Tsui F 2004 *Appl. Surf. Sci.* **223** 175
- [30] Tsui F and Ryan P A 2002 *Appl. Surf. Sci.* **189** 333
- [31] Tsui F, He L and Ma L 2002 *Mater. Res. Soc. Symp. Proc.* **700** 39
- [32] Tsui F, He L, Lorang D, Fuller A, Chu Y S, Tkachuk A and Vogt S 2006 *Appl. Surf. Sci.* **252** 2512 and references therein
- [33] Collins B A, Chu Y S, He L, Zhong Y, Vogt S and Tsui F 2008 *Phys. Rev. B* **77** 193301
- [34] Collins B A, Zhong Y, Chu Y S, He L and Tsui F 2007 *J. Vac. Sci. Technol. B* **25** 999
- [35] Birss R R 1964 *Symmetry and Magnetism* (Amsterdam: North-Holland)
- [36] You C Y and Shin S C 1996 *Appl. Phys. Lett.* **69** 1315
- [37] Qiu Z Q and Bader S D 2000 *Rev. Sci. Instrum.* **71** 1243
- [38] Muduli P K, Rice W C, He L and Tsui F 2008 *J. Magn. Magn. Mater.* **320** L141
- [39] Vavassori P 2000 *Appl. Phys. Lett.* **77** 1605
- [40] Gester M, Daboo C, Hicken R J, Gray S J, Ercole A and Bland J A C 1996 *J. Appl. Phys.* **80** 347
- [41] Florczak J M and Dahlberg E D 1991 *Phys. Rev. B* **44** 9338
- [42] Gu E, Bland J A C, Daboo C, Gester M, Brown L M, Ploessl R and Chapman J N 1995 *Phys. Rev. B* **51** 3596
- [43] Riggs K T, Dahlberg E D and Prinz G A 1990 *Phys. Rev. B* **41** 7088
- [44] Dos Santos M C, Geshev J, Schmidt J E, Teixeira S R and Pereira L G 2000 *Phys. Rev. B* **61** 1311
- [45] Rezende S M, Moura J A S, de Aguiar F M and Schreiner W H 1994 *Phys. Rev. B* **49** 15105
- [46] Višňovský Š 1986 *Czech. J. Phys.* **36** 1424
- [47] Zak J, Moog E R, Liu C and Bader S D 1990 *J. Appl. Phys.* **68** 4203